

# Multi-Scale Coherent Magnetic Field from Atomic Medium to L1544 Molecular Core

**Tao-Chung Ching** (✉ [chingtaochung@gmail.com](mailto:chingtaochung@gmail.com))

CAS Key Laboratory of FAST, NAOC, Chinese Academy of Sciences <https://orcid.org/0000-0001-8516-2532>

**Di Li**

National Astronomical Observatories, Chinese Academy of Sciences <https://orcid.org/0000-0003-3010-7661>

**Carl Heiles**

University of California, Berkeley

**Zhi-Yun Li**

University of Virginia

**Lei Qian**

National Astronomical Observatories, Chinese Academy of Sciences <https://orcid.org/0000-0003-0597-0957>

**Youling Yue**

National Astronomical Observatories, Chinese Academy of Sciences <https://orcid.org/0000-0003-4415-2148>

**Jing Tang**

National Astronomical Observatories, Chinese Academy of Sciences

**Sihan Jiao**

National Astronomical Observatories, Chinese Academy of Sciences

---

## Physical Sciences - Article

**Keywords:** magnetic fields, Zeeman measurements

**Posted Date:** March 24th, 2021

**DOI:** <https://doi.org/10.21203/rs.3.rs-343684/v1>

**License:**   This work is licensed under a Creative Commons Attribution 4.0 International License.

[Read Full License](#)

---

**Version of Record:** A version of this preprint was published at Nature on January 5th, 2022. See the published version at <https://doi.org/10.1038/s41586-021-04159-x>.

# 1 Multi-Scale Coherent Magnetic Field from Atomic Medium to 2 L1544 Molecular Core

3 T.-C. Ching<sup>1</sup>\*, D. Li<sup>1,2</sup>†, C. Heiles<sup>3</sup>, Z.-Y. Li<sup>4</sup>, L. Qian<sup>1</sup>, Y. L. Yue<sup>1</sup>, J. Tang<sup>1</sup>, S. H. Jiao<sup>1,2</sup>

4 <sup>1</sup>CAS Key Laboratory of FAST, NAOC, Chinese Academy of Sciences, Beijing 100101, China

5 <sup>2</sup>University of Chinese Academy of Sciences, Beijing 100049, China

6 <sup>3</sup>University of California, Berkeley, CA 94720, USA

7 <sup>4</sup>Astronomy Department, University of Virginia, Charlottesville, VA 22904, USA

8 **Magnetic fields play an important role in the evolution of interstellar medium and star for-**  
9 **mation** <sup>1,2</sup>. As the only direct tracer of interstellar field strength, credible Zeeman measure-  
10 **ments remain sparse due to rather limited number of spectral lines with discernible Zeeman**  
11 **effect, particularly for cold, molecular gas**<sup>3</sup>. Here we report the detection of a magnetic field  
12 **of  $3.8 \pm 0.3 \mu\text{G}$  through a new tracer, the H<sub>I</sub> narrow self-absorption (H<sub>I</sub>NSA)<sup>4,5</sup>, toward the**  
13 **prestellar core L1544 of the Taurus molecular cloud using the Five-hundred-meter Aper-**  
14 **ture Spherical radio Telescope (FAST). A combined analysis of the Zeeman measurements**  
15 **of quasar H<sub>I</sub> absorption, H<sub>I</sub> emission, OH emission, and H<sub>I</sub>NSA reveals a coherent magnetic**  
16 **field from the atomic cold neutral medium (CNM) to the molecular envelope of the L1544.**  
17 **We find that the molecular envelope traced by H<sub>I</sub>NSA is already magnetically supercritical,**  
18 **with a field strength comparable to that in the surrounding diffuse, magnetically subcriti-**  
19 **cal CNM despite a large increase in density. The reduction of the magnetic flux relative to**

---

\*Email: chingtaochung@gmail.com, orcid.org/0000-0001-8516-2532

†Email: dili@nao.cas.cn, orcid.org/0000-0003-3010-7661

20 **the mass, necessary for star formation, thus seems to happen during the transition from the**  
21 **diffuse CNM to the molecular gas traced by HiNSA , earlier than envisioned in the classical**  
22 **picture where magnetically supercritical cores capable of collapsing into stars form out of**  
23 **magnetically subcritical envelopes<sup>6,7</sup>. The HiNSA Zeeman effect opens up a new window on**  
24 **the interstellar magnetic field that is poised for rapid growth in the era of Square Kilometer**  
25 **Array and its precursors.**

26 L1544 is a well-studied prototypical low-mass prestellar core <sup>8</sup> in the Taurus molecular cloud  
27 complex at a distance of about 140 pc <sup>9</sup>. The core has a mass of 3.2 solar mass ( $M_{\odot}$ ) and a size  
28 of  $\sim 0.1$  pc <sup>10</sup>, embedded in a 30  $M_{\odot}$  envelope with a flatten shape of 1 pc along the long axis  
29 <sup>11</sup> \*. The core is characterized by a high central number density of  $\sim 2 \times 10^6$  cm<sup>-3</sup> <sup>12</sup>, a low  
30 central temperature of  $\sim 6$  K <sup>13</sup>, and strong depletion of carbon-bearing molecules <sup>14</sup>. Together  
31 with a slow infall velocity of  $\sim 0.1$  km s<sup>-1</sup> and a narrow turbulent line width of 0.2 km s<sup>-1</sup> <sup>11,14,15</sup>,  
32 comprehensive chemical and dynamical modeling suggest that L1544 could be a quiescent core in  
33 an early transition between starless and protostellar phases <sup>12,16,17</sup>.

34 We developed the so-called HiNSA technique to reveal the atomic gas well mixed with  
35 molecular gas <sup>4,5</sup> and thus provide a rare probe of the transition from H<sub>I</sub> to H<sub>2</sub>. The HiNSA feature  
36 in L1544 has a strong absorption dip and a nearly thermalized narrow line width at a temperature  
37 lower than 15 K <sup>4</sup>. The non-thermal line width and centroid velocity of the HiNSA are very close  
38 to those of the emission lines of OH, <sup>13</sup>CO, and C<sup>18</sup>O molecules, and their column densities are

---

\*In this paper, we refer to a core as an entity of dense molecular gas within a size of 0.1 pc, and an envelope as the molecular gas surrounding a core in a range of 0.1-1 pc.

39 essentially correlated<sup>5</sup>. The correlation of the line widths and column densities suggests that a  
40 significant fraction of the atomic hydrogen is located in the cold, well-shielded portions of L1544  
41 and mixed with the molecular gas, distinguished from the broader absorption features seen in other  
42 surveys of H<sub>I</sub> throughout the Galaxy.

43 The previous Zeeman observations of OH emission line toward the L1544 center detect a  
44 magnetic field strength of  $10.8 \pm 1.7 \mu\text{G}$  with the Arecibo Telescope<sup>18</sup>. However, the OH Zeeman  
45 observations of the Green Bank Telescope (GBT) toward four locations of the envelope at a radius  
46 of 6.0' (0.24 pc) from the core center yield large uncertainties in the magnetic field strengths at  
47 the four locations, and a simultaneous fit for a single strength of all four locations yields a low-  
48 confident value of  $2 \pm 3 \mu\text{G}$ , leading to debates on whether the data can be used to constrain the  
49 structure of magnetic fields in the envelope because of limited quality<sup>19–22</sup>. Since the previous  
50 Zeeman observations cannot definitively determine the magnetic field strength in the envelope,  
51 sensitive observations of Zeeman effects of a new tracer are urgently needed. Unfortunately, Zee-  
52 man measurements in interstellar medium of non-masing sources are extremely sparse, and only  
53 the tracers of H<sub>I</sub>, OH, and CN have successfully produced systematic Zeeman measurements for  
54 reasons of abundance, Zeeman splitting Landé g-factor, and excitation conditions of the tracers<sup>23</sup>.  
55 Although the Zeeman effect of H<sub>I</sub> self-absorption feature have been found towards the directions  
56 of molecular clouds<sup>24,25</sup>, the broad line widths of the absorption components are mostly asso-  
57 ciated with diffuse atomic gas rather than dense molecular gas. Considering that H<sub>I</sub> has a larger  
58 Landé g-factor than most molecules and is less affected by depletion at high densities than heav-  
59 ier molecules and that H<sub>I</sub>NSA typically has a higher brightness temperature than most molecular

60 lines, it is natural to use  $\text{H}\text{iNSA}$  to measure magnetic field strength in molecular gas.

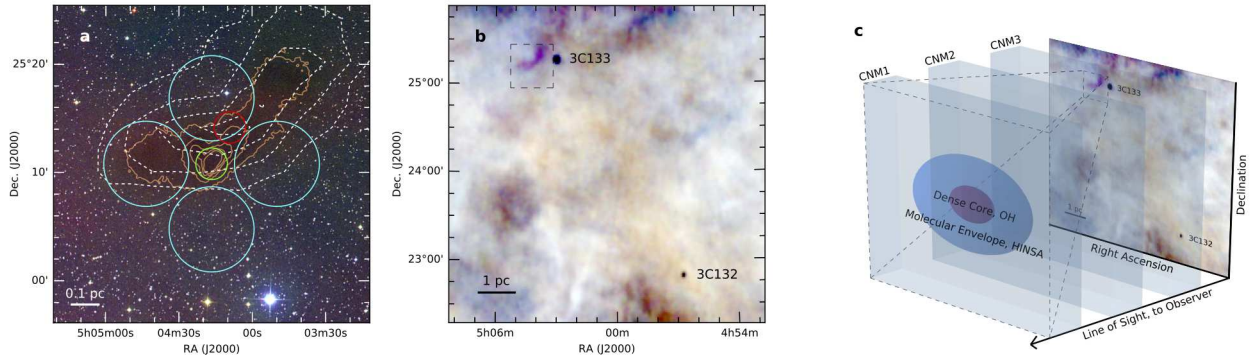


Figure 1: **L1544 core and illustration of the structure of interstellar medium from CNM to core.** **a**, a composite of DSS2 images of L1544 with *i*-band in red, *r*-band in green, and *b*-band in blue overlaid with  $\text{H}\text{iNSA}$  and  $\text{H}_2$  column density maps. White dashed contours are 30%, 50%, 70%, and 90% of the peak  $\text{H}\text{iNSA}$  column density, and orange contours are  $2, 4, 6, 8, 10 \times 10^{21} \text{ cm}^{-2}$  for the  $\text{H}_2$  column density. The red, green, and cyan circles mark the locations and beam sizes of the FAST, Arecibo, and GBT Zeeman observations, respectively. **b**, a composite of three  $0.5 \text{ km s}^{-1}$  velocity slices of Arecibo GALFA- $\text{H}\text{i}$  images at  $6.2, 6.7,$  and  $7.3 \text{ km s}^{-1}$  LSR velocities in blue, green, and red. The dashed rectangle shows the region of **a**. The two absorption dots represent the locations of quasars 3C132 and 3C133. **c**, schematic view of CNMs, molecular envelope, and L1544 core.

61 We detected Zeeman splittings toward the  $\text{H}\text{iNSA}$  column density peak at a distance of  $3.6'$   
 62 ( $0.15 \text{ pc}$ ) away from the L1544 center (Fig. 1) at an angular resolution of  $2.9'$  ( $0.12 \text{ pc}$ ) with  
 63 FAST<sup>26</sup>. The spectra of the Stokes  $I(\nu)$  and  $V(\nu)$  parameters (where  $\nu$  denotes velocity) at 21-cm  
 64 wavelength are shown in Fig. 2. The  $I(\nu)$  spectrum contains  $\text{H}\text{i}$  emission of CNM and warm neu-  
 65 tral medium (WNM) clouds in the direction toward the Taurus complex and a  $\text{H}\text{iNSA}$  feature at

66 the centroid velocity of L1544. Least-squares fits of multiple gaussians with radiative transfer de-  
67 compose the  $I(v)$  into a foreground HiNSA component, a background WNM component, and three  
68 CNM components between the HiNSA and WNM. The fitted  $I(v)$  profiles of the HiNSA , CNM,  
69 and WNM components are shown in Fig. 2a. Our fitted parameters of the HiNSA component are  
70 in good agreement with the previous HiNSA observations <sup>4,5</sup>, and our parameters of the CNM and  
71 WNM components are similar to the Arecibo results toward quasars around L1544 <sup>27</sup>.

72 The  $V(v)$  spectrum shows features of classic ‘S curve’ patterns proportional to the first deriva-  
73 tives of  $I(v)$  for the HiNSA , CNM, and WNM components, as expected for Zeeman splittings. The  
74 Zeeman splitting profile of HiNSA has a maximum at high velocity and a minimum at low veloc-  
75 ity, opposite to the Zeeman splitting profile of CNM1, the closest CNM component at a velocity  
76 similar to L1544, that shows positive  $V$  at low velocity and negative  $V$  at high velocity. From our  
77 least-squares fits to  $V(v)$ , we obtain the magnetic field strengths of the HiNSA , CNM, and WNM  
78 components, listed in Table 2 of Methods. The fitted  $V(v)$  profile of the HiNSA and the total  $V(v)$   
79 profile of the five components are show in Fig. 2b, and the individual  $V(v)$  profiles of the compo-  
80 nents are shown in Fig. 3. The HiNSA Zeeman effect gives  $B_{los} = 3.8 \pm 0.3 \mu\text{G}$ , and the Hi Zeeman  
81 effect of CNM1 gives  $B_{los} = 4.0 \pm 1.1 \mu\text{G}$ , where  $B_{los}$  is the magnetic field component projected  
82 along the line of sight with positive sign representing field pointing away from the observer. The  
83 magnetic field strengths of HiNSA and CNM1 are consistent with the results of  $B_{los} = 5.8 \pm 1.1 \mu\text{G}$   
84 and  $4.2 \pm 1.0 \mu\text{G}$  obtained from the Zeeman observations toward quasars 3C133 and 3C132, prob-  
85 ing the magnetic fields of CNM1 at velocities of  $8.0 \pm 0.0 \text{ km s}^{-1}$  and  $8.1 \pm 0.0 \text{ km s}^{-1}$  at distances  
86 of 17.7’ (0.72 pc) and 174.5’ (7.1 pc) from L1544, respectively <sup>28</sup>. In addition, the weak strengths

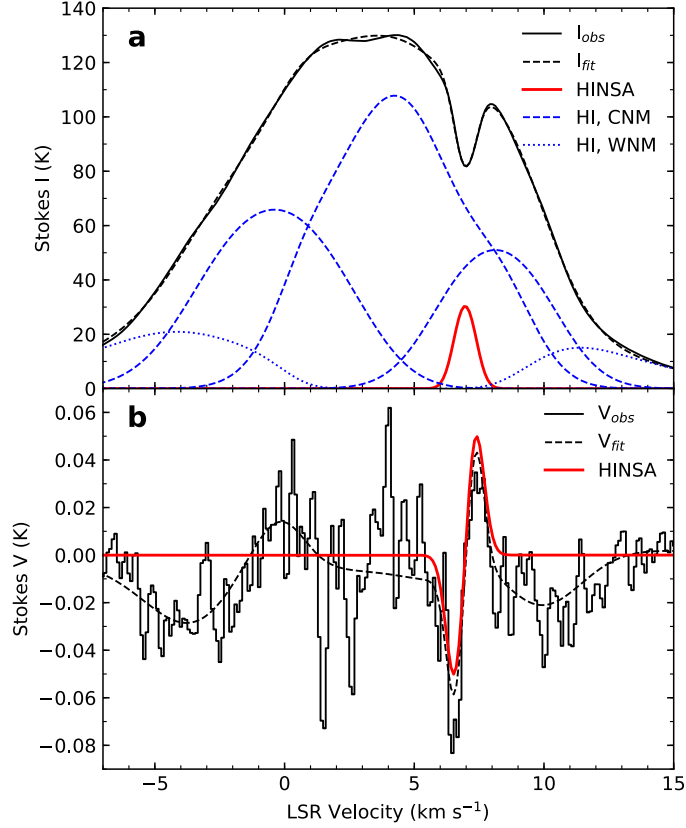


Figure 2: **The Stokes  $I(v)$  and  $V(v)$  spectra at 21-cm wavelength toward the HiNSA column density peak.** **a**, The black profile represents the  $I(v)$  spectrum. The red profile represents the absorption from the foreground HiNSA component. The blue dashed and dotted profiles represent the emission of the CNM and WNM components, respectively. The CNM and WNM profiles include the absorption from the CNM components that lie in front but not include the absorption from HiNSA. The black dashed profile represents the sum of the absorption and emission profiles. **b**, The black profile represents the  $V(v)$  spectrum. The black dashed profile represents the sum of the Zeeman splitting profiles of the five components. The red profile represents the Zeeman splitting profile with  $B_{los} = 3.8 \mu\text{G}$  of the HiNSA component.

87 inferred from Zeeman measurements are broadly consistent with the large dispersion of  $H$ -band  
 88 polarization angles in the envelope of L1544<sup>29</sup>, given that near-infrared polarimetry traces the  
 89 magnetic field component projected on the plane of sky and field strength is inversely proportional  
 90 to the dispersion of polarization angles. For the second and third CNM components (CNM2 and  
 91 CNM3) along the line of sight, our results of  $B_{los,CNM2} = -7.6 \pm 1.0 \mu\text{G}$  and  $B_{los,CNM3} = 2.9 \pm 0.4$   
 92  $\mu\text{G}$  are also consistent with the results of  $B_{los,CNM2} = -9.6 \pm 6.3 \mu\text{G}$  and  $B_{los,CNM3} = -0.3 \pm 1.7 \mu\text{G}$   
 93 toward quasar 3C133<sup>28</sup>.

94 Comparing the Zeeman observations of H<sub>I</sub>NSA, OH, and H<sub>I</sub> tracing the CNM1 and the  
 95 molecular envelope of L1544, it is clear that the magnetic fields at distances of 0.15, 0.24, 0.72,  
 96 and 7.1 pc from the center all have the same direction of  $B_{los}$  and consistent strengths roughly  
 97 within the  $1\sigma$  uncertainty in each measurement. Owing to the different excitation conditions and  
 98 abundances of the three tracers, the H<sub>I</sub> absorptions toward 3C133 and 3C132 trace CNM with a  
 99 kinematic temperature of about 100 K<sup>28</sup> and a number density of about  $50 \text{ cm}^{-3}$ <sup>23</sup>, whereas the  
 100 H<sub>I</sub>NSA and OH observations trace the envelope of L1544 with a kinematic temperature of about  
 101 10–15 K<sup>4</sup> and a number density at the order of  $10^3 \text{ cm}^{-3}$ <sup>5,23</sup>. Despite the 1-2 orders of magnitude  
 102 change in both temperature and density in the phase transition from the atomic CNM to the molec-  
 103 ular envelope, the Zeeman observations reveal a magnetic field that is coherent in both direction  
 104 and strength across multi-scales and multi-phases of the interstellar medium. Note that the mag-  
 105 netic field is also coherent in the line of sight, since the FAST results of H<sub>I</sub>NSA and H<sub>I</sub> indicate  
 106 consistent  $B_{los}$  at different depths of clouds along the line of sight. To constrain the uniformity  
 107 of the coherent magnetic field, we performed a likelihood analysis with the assumption that the

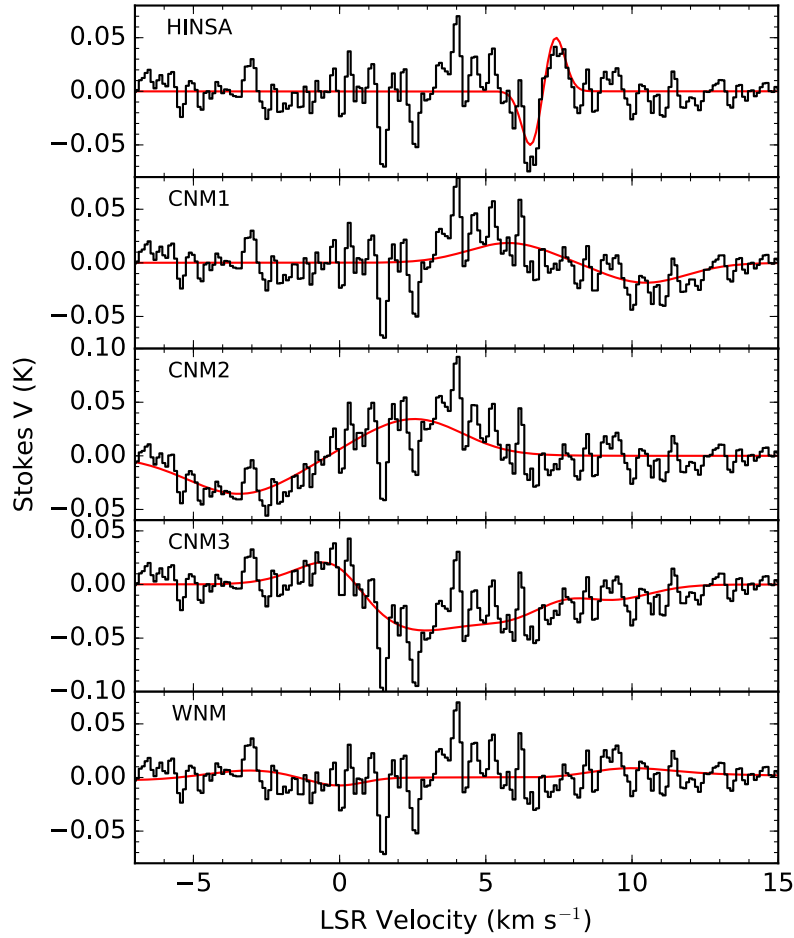


Figure 3: **The individual  $V(v)$  profiles for the HINSA , CNM, and WNM components.** In each panel, the red profile represents the fitted Zeeman profile of the component, and the black profile represents the observed  $V(v)$  subtracted by the fitted Zeeman profiles of the other four components. The CNM and WNM Zeeman profiles include the absorption from the CNM components that lie in front but not include the absorption from HINSA . The sum of the red profiles of the five components is the black dashed profile in Fig. 2b.

108  $B_{los}$  of the coherent field follows a gaussian distribution with mean  $B_0$  and intrinsic spread  $\sigma_0$ .

109 Using the HINSA , OH, and H I Zeeman measurements, the maximum likelihood parameters are

110  $B_0 = 4.1 \pm 1.6 \mu\text{G}$  and  $\sigma_0 = 1.2_{-0.6}^{+1.2} \mu\text{G}$ , providing a better constraint of the field uniformity than  
111 the previous estimation of  $B_0 = 4_{-8}^{+10} \mu\text{G}$  by using only the OH results <sup>21</sup>.

112 The Zeeman observations show that the magnetic fields from CNM to envelope are coherent  
113 and significantly weaker than the field in the core from the Arecibo OH Zeeman measurements.  
114 This finding is in agreement with the conclusion of comprehensive H<sub>I</sub>, OH, and CN Zeeman  
115 surveys, which suggest that the magnetic fields in H<sub>I</sub> clouds have a median value of 6  $\mu\text{G}$  in total  
116 strength and do not scale vary significantly with density, whereas the magnetic fields in molecular  
117 clouds tend to increase with density above a critical number density of about 300  $\text{cm}^{-3}$  <sup>23</sup>. The  
118 H<sub>I</sub>NSA column densities of L1544 are correlated with those of <sup>13</sup>CO, which typically traces a  
119 number density of a few thousand  $\text{cm}^{-3}$ . Since the H<sub>I</sub>NSA has a relatively weak magnetic field  
120 that has yet to increase beyond the values observed in the more diffuse gas, its density must be  
121 less than the critical density above which the field strength starts to increase with density. In  
122 other words, the H<sub>I</sub>NSA observations suggest a critical density of at least a few thousand  $\text{cm}^{-3}$   
123 in the L1544 system, which provides an important connection between the magnetic fields from  
124 H<sub>I</sub> clouds to molecular clouds that was not available before.

125 It is well known that the progenitor of molecular gas, the atomic CNM, is strongly mag-  
126 netized, as measured by the dimensionless mass-to-magnetic flux ratio  $\lambda$  in units of the critical  
127 value of  $2\pi G^{1/2}$  ( $\lambda = 7.6 \times 10^{-21} [N/\text{cm}^{-2}][B/\mu\text{G}]^{-1}$ ), which is well below unity (i.e., magneti-  
128 cally subcritical) <sup>30</sup>. On the other hand, the immediate progenitors of stars, the prestellar cores of  
129 molecular clouds such as the L1554 core, are observed to be magnetically supercritical ( $\lambda > 1$ ) <sup>18</sup>,

130 which is required for the self-gravity to overwhelm the magnetic support and form stars through  
131 gravitational collapse. When and how the transition from the magnetically subcritical CNM that  
132 is incapable of forming stars through direct gravitational collapse to the supercritical star-forming  
133 cores is a central unresolved question in star formation.

134 Our HiNSA Zeeman observations can be used to address this question. Using the physical  
135 parameters of the clouds (Table 1) and the statistically most probable value of the total field strength  
136  $B = 2B_{los}$ , the  $\lambda$  of CNM1 is about 0.19–0.37, consistent with previous results<sup>30</sup>. The  $\lambda$  of  
137 the envelope and core of L1544 core is 2.5–3.5, which is well above unity, indicating that the  
138 transition to magnetic supercriticality has already occurred. Because the magnetic fields from  
139 CNM to envelope are coherent, the angles between the line of sight and  $B$  in the clouds should  
140 be similar. The relative values of  $\lambda$  between CNM1 and L1544 thus is considered to avoid the  
141 uncertainty in the geometrical correction from  $B_{los}$  to  $B$ <sup>19</sup>. Therefore, the molecular envelope  
142 of the L1544 core traced by HiNSA is at least 6 times less magnetized relative to its mass (as  
143 measured by  $\lambda$ ) compared to its ambient CNM. This is different from the classic theory of low-  
144 mass star formation, which envisions the transition from magnetic subcriticality to supercriticality  
145 occurring as the supercritical core forms out of the magnetically supported (subcritical) envelope  
146<sup>6,7</sup>. Our results suggest that the transition to supercriticality occurs earlier, during the formation  
147 of the molecular envelope. In other words, by the time that the molecular envelope is formed, the  
148 problem of excessive magnetic flux as a fundamental obstacle to gravitational collapse and star  
149 formation is already resolved. The already magnetically supercritical envelope can in principle  
150 go on to form dense cores without having to reduce its magnetic flux relative to mass further, as

151 indicated by the comparable values of  $\lambda$  ( $\sim 3$ ) for both the molecular envelope and core of L1544  
 152 (see Table 1).

Table 1: **Physical Parameters of the Clouds**

Tracer/Cloud	$B_{los}$ [ $\mu\text{G}$ ]	$N$ [ $10^{20} \text{ cm}^{-2}$ ]	$\lambda$
H <sub>3</sub> C <sub>132</sub> /CNM1	$4.2 \pm 1.0$	$4.05 \pm 1.07$ <sup>†</sup>	$0.37 \pm 0.13$
H <sub>3</sub> C <sub>133</sub> /CNM1	$5.8 \pm 1.1$	$2.89 \pm 1.03$ <sup>†</sup>	$0.19 \pm 0.08$
HiNSA/envelope	$3.8 \pm 0.3$	$34.9 \pm 0.1$ <sup>‡</sup>	$3.5 \pm 0.3$
OH/core	$10.8 \pm 1.7$	$70.5 \pm 0.2$ <sup>‡</sup>	$2.5 \pm 0.4$

153 <sup>†</sup> Ref. 26.

154 <sup>‡</sup> Obtained from the H<sub>2</sub> column density map in Fig. 1a.

155 In summary, the HiNSA Zeeman observations reveal a coherent magnetic field from CNM  
 156 to the envelope of a prestellar core, providing an important connection between the magnetic  
 157 fields from H<sub>I</sub> clouds to molecular clouds. HiNSA has features of strong absorption and narrow  
 158 linewidth, making the Zeeman effect of HiNSA prominent and relatively easy to identify. In ad-  
 159 dition, the detection rate of HiNSA in dense cores and their molecular envelopes is high, and the  
 160 foreground/background confusion in HiNSA is minimized since the foreground gas usually has  
 161 a small optical depth <sup>4</sup>. Therefore, HiNSA has a great potential to become the fourth tracer to  
 162 perform systematic Zeeman observations. Future HiNSA Zeeman observations toward multiple  
 163 locations of prestellar cores will reveal more details of magnetic field structures, offering guidance

164 on deciphering the role of magnetic fields in star formation.

- 168 1. McKee, C. F. & Ostriker, E. C. Theory of Star Formation. ARA&A **45**, 565–687 (2007).  
167 0707.3514.
- 168 2. Hennebelle, P. & Inutsuka, S.-i. The role of magnetic field in molecular cloud formation and  
169 evolution. Frontiers in Astronomy and Space Sciences **6**, 5 (2019). 1902.00798.
- 170 3. Crutcher, R. M. & Kemball, A. J. Review of Zeeman Effect Observations of Regions of  
171 Star Formation K Zeeman Effect, Magnetic Fields, Star formation, Masers, Molecular clouds.  
172 Frontiers in Astronomy and Space Sciences **6**, 66 (2019). 1911.06210.
- 173 4. Li, D. & Goldsmith, P. F. H I Narrow Self-Absorption in Dark Clouds. ApJ **585**, 823–839  
174 (2003). astro-ph/0206396.
- 175 5. Goldsmith, P. F. & Li, D. H I Narrow Self-Absorption in Dark Clouds: Correlations with  
176 Molecular Gas and Implications for Cloud Evolution and Star Formation. ApJ **622**, 938–958  
177 (2005). astro-ph/0412427.
- 178 6. Shu, F. H., Adams, F. C. & Lizano, S. Star formation in molecular clouds: observation and  
179 theory. ARA&A **25**, 23–81 (1987).
- 180 7. Mouschovias, T. C. & Ciolek, G. E. Magnetic Fields and Star Formation: A Theory Reaching  
181 Adulthood. In Lada, C. J. & Kylafis, N. D. (eds.) The Origin of Stars and Planetary Systems,  
182 vol. 540 of NATO Advanced Study Institute (ASI) Series C, 305 (1999).
- 183 8. Snell, R. L. A study of nine interstellar dark clouds. ApJS **45**, 121–175 (1981).

- 184 9. Elias, J. H. A study of the Taurus dark cloud complex. ApJ **224**, 857–872 (1978).
- 185 10. Ward-Thompson, D., Motte, F. & Andre, P. The initial conditions of isolated star formation -  
186 III. Millimetre continuum mapping of pre-stellar cores. MNRAS **305**, 143–150 (1999).
- 187 11. Tafalla, M. et al. L1544: A Starless Dense Core with Extended Inward Motions. ApJ **504**,  
188 900–914 (1998).
- 189 12. Aikawa, Y., Ohashi, N., Inutsuka, S.-i., Herbst, E. & Takakuwa, S. Molecular Evolution in  
190 Collapsing Prestellar Cores. ApJ **552**, 639–653 (2001). [astro-ph/0202061](#).
- 191 13. Crapsi, A., Caselli, P., Walmsley, M. C. & Tafalla, M. Observing the gas temperature drop in  
192 the high-density nucleus of L 1544. A&A **470**, 221–230 (2007). [0705.0471](#).
- 193 14. Tafalla, M., Myers, P. C., Caselli, P., Walmsley, C. M. & Comito, C. Systematic Molecular  
194 Differentiation in Starless Cores. ApJ **569**, 815–835 (2002). [astro-ph/0112487](#).
- 195 15. Caselli, P. et al. Molecular Ions in L1544. I. Kinematics. ApJ **565**, 331–343 (2002).  
196 [astro-ph/0109021](#).
- 197 16. Li, Z.-Y., Shematovich, V. I., Wiebe, D. S. & Shustov, B. M. A Coupled Dynamical and  
198 Chemical Model of Starless Cores of Magnetized Molecular Clouds. I. Formulation and Initial  
199 Results. ApJ **569**, 792–802 (2002). [astro-ph/0201019](#).
- 200 17. Keto, E., Caselli, P. & Rawlings, J. The dynamics of collapsing cores and star formation.  
201 MNRAS **446**, 3731–3740 (2015). [1410.5889](#).

- 202 18. Crutcher, R. M. & Troland, T. H. OH Zeeman Measurement of the Magnetic Field in the  
203 L1544 Core. ApJL **537**, L139–L142 (2000).
- 204 19. Crutcher, R. M., Hakobian, N. & Troland, T. H. Testing Magnetic Star Formation Theory.  
205 ApJ **692**, 844–855 (2009). 0807.2862.
- 206 20. Crutcher, R. M., Hakobian, N. & Troland, T. H. Self-consistent analysis of OH Zeeman  
207 observations. MNRAS **402**, L64–L66 (2010). 0912.3024.
- 208 21. Mouschovias, T. C. & Tassis, K. Testing molecular-cloud fragmentation theories: self-  
209 consistent analysis of OH Zeeman observations. MNRAS **400**, L15–L19 (2009). 0909.2031.
- 210 22. Mouschovias, T. C. & Tassis, K. Self-consistent analysis of OH-Zeeman observations: too  
211 much noise about noise. MNRAS **409**, 801–807 (2010). 1007.3741.
- 212 23. Crutcher, R. M., Wandelt, B., Heiles, C., Falgarone, E. & Troland, T. H. Magnetic Fields in  
213 Interstellar Clouds from Zeeman Observations: Inference of Total Field Strengths by Bayesian  
214 Analysis. ApJ **725**, 466–479 (2010).
- 215 24. Goodman, A. A. & Heiles, C. The Magnetic Field in the Ophiuchus Dark Cloud Complex.  
216 ApJ **424**, 208 (1994).
- 217 25. Heiles, C. A Holistic View of the Magnetic Field in the Eridanus/Orion Region. ApJS **111**,  
218 245–288 (1997).

- 219 26. Li, D. et al. FAST in Space: Considerations for a Multibeam, Multipurpose Survey Using  
220 China's 500-m Aperture Spherical Radio Telescope (FAST). IEEE Microwave Magazine **19**,  
221 112–119 (2018). 1802.03709.
- 222 27. Heiles, C. & Troland, T. H. The Millennium Arecibo 21 Centimeter Absorption-Line Survey.  
223 I. Techniques and Gaussian Fits. ApJS **145**, 329–354 (2003). astro-ph/0207104.
- 224 28. Heiles, C. & Troland, T. H. The Millennium Arecibo 21 Centimeter Absorption-Line Survey.  
225 III. Techniques for Spectral Polarization and Results for Stokes V. ApJS **151**, 271–297 (2004).
- 226 29. Clemens, D. P., Tassis, K. & Goldsmith, P. F. The Magnetic Field of L1544. I. Near-infrared  
227 Polarimetry and the Non-uniform Envelope. ApJ **833**, 176 (2016). 1610.05543.
- 228 30. Heiles, C. & Troland, T. H. The Millennium Arecibo 21 Centimeter Absorption-Line Survey.  
229 IV. Statistics of Magnetic Field, Column Density, and Turbulence. ApJ **624**, 773–793 (2005).  
230 astro-ph/0501482.

231 **Acknowledgements** This work is supported by the National Natural Science Foundation of China (NSFC)  
232 grant No. 11988101, U1931117, and 11725313; by CAS International Partnership Program No.  
233 114A11KYSB20160008; and by the National Key R&D Program of China No. 2017YFA0402600. T.-C.  
234 C. is funded by Chinese Academy of Sciences Taiwan Young Talent Program. Grant No.2018TW2JB0002.  
235 T.-C. C. and J. T. are supported by Special Funding for Advanced Users, budgeted and administrated by  
236 Center for Astronomical Mega-Science (CAMS), Chinese Academy of Sciences. C. H. is funded by Chinese  
237 Academy of Sciences President's International Fellowship Initiative Grant No. 2020DM0005. Z.-Y. L. is  
238 supported in part by NASA 80NSSC20K0533 and NSF AST-1716259 and 1815784. This work made use of

239 data from FAST, a Chinese national mega-science facility built and operated by the National Astronomical  
240 Observatories, Chinese Academy of Sciences.

241 **Author Contributions** T.-C. C., D. L., and C. H. launched the FAST Zeeman project; T.-C. C. processed  
242 the data and analysis in consultation with C. H.; T.-C. C., Z.-Y. L., D. L., and C. H. drafted the paper; L.  
243 Q., Y. L. Y. , and J. T. made key contributions to arrange the FAST observations of L1544 and polarization  
244 calibration; S. H. J. provided the H<sub>2</sub> column density map.

245 **Competing Interests** The authors declare that they have no competing financial interests.

## 246 **Methods**

247 **Data reduction** The FAST Zeeman observations toward the H<sub>I</sub>NSA column density peak in L1544  
248 were carried out in 5 days in August, September, and November 2019 with a total integration time  
249 of 7.6 hours. The H<sub>I</sub>NSA spectra were obtained with the central beam of the L-band 19-beam  
250 receiver<sup>31</sup>. The central beam has an average system temperature of 24 K, a main beam efficiency  
251 of 0.63, and a main beam diameter at the half-power point of 2.9' with a pointing accuracy of  
252 7.9". The 19-beam receiver had orthogonal linear polarization feeds followed by a temperature  
253 stabilized noise injection system and low noise amplifiers to produce the X and Y signals of the  
254 two polarization paths. The XX, YY, XY, and YX correlations of the signals then were simultane-  
255 ously recorded using the ROACH backend with 65536 spectral channels in each polarization. The  
256 spectral bandwidth was 32.75 MHz centered at the frequency of the H<sub>I</sub> 21-cm line for a channel  
257 spacing of 500 Hz, and the  $V(\nu)$  spectrum presented in this work was Hanning-smoothed, which  
258 produced a spectral resolution of 0.21 km s<sup>-1</sup>.

259 The data reduction including gain and phase calibrations of the two polarization paths, band-  
260 pass calibrations of the four correlated spectra, and polarization calibrations to generate Stokes  $I$ ,  
261  $Q$ ,  $U$ , and  $V$  spectra was made with the IDL RHSTK package written by C. Heiles and T. Robshaw  
262 that is widely used for Arecibo and GBT polarization data. The 19-beam receiver is rotatable from  
263 -80° to +80° with respect to the line of equatorial latitude. The polarization calibrations used drift-  
264 ing scans of the continuum source 3C286 at rotation angles of -60°, -30°, 0°, 30°, and 60° over  
265 1.5 hours surrounding its transit. The details of the polarization calibration procedure were pro-  
266 vided in<sup>32</sup>. We performed polarization calibrations once a month during the observations. The

267 calibrated polarization of 3C286 of the three epochs were  $8.9\% \pm 0.1\%$ ,  $8.7\% \pm 0.2\%$ , and  $9.0\%$   
268  $\pm 0.1\%$  for polarization degrees and  $30.4^\circ \pm 0.3^\circ$ ,  $33.8^\circ \pm 0.5^\circ$ , and  $29.4^\circ \pm 0.3^\circ$  for polarization  
269 angles. Considering that the ionosphere can generate a faraday rotation of  $1^\circ\text{--}3^\circ$  in polarization  
270 angle at L-band <sup>33</sup>, our results were consistent with the intrinsic polarization degree of  $9.5\%$  and  
271 polarization angle of  $33^\circ$  of 3C286 at 1450 MHz <sup>34</sup>. In addition to the polarization observations of  
272 L1544 and 3C286, we observed the circularly polarized OH maser source IRAS02524+2046 <sup>35</sup> in  
273 order to verify that our procedures produced consistent  $B_{los}$ , including the sign or direction of the  
274 magnetic field, as had been obtained previously.

275 The convolutions of the sidelobes of the Stokes  $V$  beam with the spatial gradient of the Stokes  
276  $I$  emission may generate a false ‘S curve’ in the  $V$  spectrum <sup>28</sup>. In order to check the credibility  
277 of our Zeeman detections, we measured the Stokes  $V$  beam of FAST and convolved the beam with  
278 the GALFA Stokes  $I$  cube <sup>36</sup> of L1544. The convolved  $V$  spectrum showed a profile with a shape  
279 similar to the  $I$  spectrum and a strength less than  $0.03\%$  of the  $I$  spectrum, different from the ‘S  
280 curve’ patterns in the observed  $V$  spectrum. Meanwhile, the 19-beam receiver was rotated to  $-45^\circ$ ,  
281  $0^\circ$ , and  $45^\circ$  in the three epochs of the L1544 observations, and all of the three epochs showed ‘S  
282 curve’ patterns in the  $V$  spectra, indicating that our Zeeman results were true detections.

283 **Multiple gaussians and radiative transfer fitting to  $I(\mu)$  and  $V(\mu)$**  Our fitting of  $I(\nu)$  adopts the  
284 equations of gaussian components and radiative transfer <sup>27</sup>. The expected profile of  $I(\nu)$  consists  
285 of multiple CNM components providing opacity and also brightness temperature and a WNM

286 component providing only brightness temperature:

$$I(\nu) = I_{CNM}(\nu) + I_{WNM}(\nu). \quad (1)$$

287 The  $I_{CNM}(\nu)$  is an assembly of  $N$  CNM components

$$I_{CNM}(\nu) = \sum_{n=1}^N I_{peak,n} (1 - e^{-\tau_n(\nu)}) e^{-(\sum_{m=1}^M \tau_m(\nu) + \tau_0)}, \quad (2)$$

288 where the subscript  $m$  with its associated optical depth profile  $\tau_m(\nu)$  represents each of the  $M$  CNM  
289 clouds that lie in front of cloud  $n$ . The optical depth of the  $i$ th component is

$$\tau_i(\nu) = \tau_i e^{-[(\nu - \nu_{0,i})/\sigma_{\nu,i}]^2} \quad (3)$$

290 in which  $\tau_0$  represents the HNSA providing only opacity and no brightness temperature. For the  
291 WNM in the background,

$$I_{WNM}(\nu) = I_{peak,WNM} e^{-[(\nu - \nu_{0,WNM})/\sigma_{\nu,WNM}]^2} e^{-\sum_{i=0}^N \tau_i(\nu)}. \quad (4)$$

292 The fitting of  $I(\nu)$  thus yields values for  $I_{peak}$ ,  $\tau$ ,  $\nu_0$ , and  $\sigma_\nu$  of the components.

293 We consider the radiative transfer of  $V(\nu)$  in terms of right circular polarization (RCP) and  
294 left circular polarization (LCP). The Zeeman effect states that with the existence of  $B_{los}$ , the fre-  
295 quency of RCP shifts from its original frequency  $\nu_0$  to  $\nu_0 + \nu_z$  and the frequency of LCP shifts  
296 to  $\nu_0 - \nu_z$  with  $\nu_z = (Z/2) \times B_{los}$ , where  $Z$  is the Zeeman splitting factor (2.8 Hz  $\mu\text{G}^{-1}$  for H<sub>I</sub>21-  
297 cm line). Since the RCP and LCP are orthogonal components of radiation, the radiative transfer  
298 processes of RCP and LCP are independent to each other. For RCP, Equation (1) becomes

$$T_{RCP} = T_{RCP,CNM}(\nu, \tau_{RCP,i}) + T_{RCP,WNM}(\nu, \tau_{RCP,i}), \quad (5)$$

299 where for the  $i$ th component,  $T_{RCP,i} = I_{peak,i}/2$ ,  $\tau_{RCP,i}$  is optical depth in the RCP radiation to  
 300 substitute the  $\tau_i$  in Equation (3) with  $\tau_{RCP,i} = \tau_i(v_0 + v_{z,i})$  for  $B_{los,i}$  of the component, and the  
 301 parameters of  $v_0$  and  $\sigma_v$  keep the same. Similarly, for LCP,

$$T_{LCP} = T_{LCP,CNM}(v, \tau_{LCP,i}) + T_{LCP,WNM}(v, \tau_{LCP,i}) \quad (6)$$

302 with  $T_{LCP,i} = I_{peak,i}/2$  and  $\tau_{LCP,i} = \tau_i(v_0 - v_{z,i})$ . The fitting of  $V(v) = T_{RCP} - T_{LCP} + cI(v)$ , which  
 303 includes a  $c$  term accounting for leakage of  $I(v)$  into  $V(v)$ , thus yields values for  $B_{los}$  of the com-  
 304 ponents. In Table 2, we list the parameters of the components obtained from least-squares fits to  
 305  $I(v)$  and  $V(v)$ . The leakage of our HiNSA Zeeman observations is  $c = 0.034\%$ .

Table 2: **Gaussian Fit Parameters**

Component	$I_{peak}$ [K] <sup>a</sup>	$\tau$ <sup>b</sup>	$v_{LSR}$ [km s <sup>-1</sup> ] <sup>c</sup>	$\sigma_v$ [km s <sup>-1</sup> ] <sup>d</sup>	$B_{los}$ [ $\mu$ G]	Order <sup>e</sup>
HiNSA	–	$0.32 \pm 0.01$	$6.97 \pm 0.01$	$0.40 \pm 0.01$	$3.8 \pm 0.3$	0
CNM1	$90.34 \pm 5.49$	$0.83 \pm 0.12$	$8.12 \pm 0.11$	$1.86 \pm 0.05$	$4.0 \pm 1.1$	1
CNM2	$116.33 \pm 1.78$	$0.84 \pm 0.08$	$-0.39 \pm 0.33$	$2.41 \pm 0.13$	$-7.6 \pm 1.0$	2
CNM3	$135.31 \pm 2.04$	$10.45 \pm 0.95$	$4.38 \pm 0.09$	$2.04 \pm 0.06$	$2.9 \pm 0.4$	3
WNM	$46.70 \pm 2.47$	–	$2.63 \pm 0.04$	$6.44 \pm 0.09$	$3.0 \pm 1.7$	4

306 <sup>a</sup>  $I_{peak}$  is the intrinsic peak Stokes  $I$  emission. We do not fit  $I_{peak}$  for HiNSA because it is an absorption component.

307 <sup>b</sup>  $\tau$  is the central opacity. We do not fit  $\tau$  for WNM because it is a background component.

308 <sup>c</sup>  $v_{LSR}$  is the central LSR velocity.

309 <sup>d</sup>  $\sigma_v$  is the gaussian dispersion.

310 <sup>e</sup> The order of the component along the line of sight. Order begins with 0, and increasing numbers mean increasing

311 distance along the line of sight.

312 **HiNSA and H<sub>2</sub> column density maps** We show the HiNSA and H<sub>2</sub> column density maps of  
313 L1544 in Fig. 1a, and we use the H<sub>2</sub> column density map to calculate the  $N$  at the beams of  
314 FAST and Arecibo observations in Table 1. The HiNSA column density map is a revision of the  
315 Fig. 8 in ref. 14. To derive the H<sub>2</sub> column density map, we retrieved the level 2.5 processed,  
316 archival Herschel images that were taken at 250/350/500  $\mu\text{m}$  using the SPIRE instrument <sup>37</sup>, (ob-  
317 sid: 1342204842). We smoothed the Herschel images to a common angular resolution of the 36''  
318 beam at 500  $\mu\text{m}$  and regridded the images to the same pixel size of 6''. We performed least-squares  
319 fits of the 250/350/500  $\mu\text{m}$  spectral energy distributions weighted by the squares of the measured  
320 noise levels to derive the pixel-to-pixel distributions of dust temperature  $T_d$  and dust optical depth  
321  $\tau_\nu$  using  $S_\nu = \Omega_m B_\mu(T_d)(1 - e^{-\tau_\nu})$ , where  $S_\nu$  is the flux density at frequency  $\nu$ ,  $\Omega_m$  is the  
322 solid angle of the pixel,  $B_\mu(T_d)$  is the Planck function at  $T_d$ , and  $\tau_\nu = \tau_{230}(\nu[\text{GHz}]/230)^\beta$  with dust  
323 opacity index  $\beta$  of 1.8. Next, we obtained the H<sub>2</sub> column density with  $N = g\tau_{230}/(\kappa_{230}\mu_m m_H)$ ,  
324 where  $g = 100$  is the gas-to-dust mass ratio,  $\kappa_{230} = 0.09 \text{ cm}^2 \text{ g}^{-2}$  <sup>38</sup> is the dust opacity at 230  
325 GHz,  $\mu_m = 2.8$  is the the mean molecular weight, and  $m_H$  is the atomic mass of hydrogen. To  
326 estimate the uncertainties in the H<sub>2</sub> column density, we used a Monte-Carlo technique. For each  
327 pixel, we created artificial 250/350/500  $\mu\text{m}$  flux densities by adding the original flux densities with  
328 normal-distributed errors taking account the uncertainty in the measured flux and a 10% correlation  
329 for the calibration uncertainty in SPIRE <sup>39</sup>. We then estimated the uncertainty in each pixel with  
330 1000 fittings of the H<sub>2</sub> column density. The  $N$  and its uncertainty in Table 1 were obtained from  
331 the convolutions of the H<sub>2</sub> column density map and uncertainty map with the FAST and Arecibo

332 beams.

333 **Maximum likelihood** We adopt the analysis of maximum likelihood <sup>21</sup> to study the uniformity  
 334 of magnetic fields in the envelope of L1544. Assuming that the true  $B_{los}$  follows a gaussian dis-  
 335 tribution with mean  $B_0$  and intrinsic spread  $\sigma_0$ , the likelihood  $l_j$  for a single observation to mea-  
 336 sure  $B_j$  with gaussian error  $\sigma_j$  is proportional to the convolution of the probability  $\exp[-(B -$   
 337  $B_0)^2/2\sigma_0^2]/\sqrt{2\pi}\sigma_0$  for the magnetic field to have a true value of  $B$  with the probability  $\exp[-(B -$   
 338  $B_j)^2/2\sigma_j^2]/\sqrt{2\pi}\sigma_j$  of observing a value  $B_j$  of the field. Therefore,  $l_j$  is the integral over all possible  
 339 true values of the magnetic field

$$l_j = \int_{-\infty}^{\infty} dB \frac{\exp[-(B - B_j)^2/2\sigma_j^2] \exp[-(B - B_0)^2/2\sigma_0^2]}{\sqrt{2\pi}\sigma_j \sqrt{2\pi}\sigma_0}. \quad (7)$$

340 While the overall likelihood  $\mathcal{L}$  for a set of observations is the product of individual like-  
 341 lihoods of the observations ( $\mathcal{L} = \prod_{j=1}^N l_j$ ), the  $B_0$  and  $\sigma_0$  can be estimated by maximizing the  
 342 likelihood  $\mathcal{L}$ . After performing the integration in Equation (7) and some algebraic manipulations,

$$\mathcal{L}(B_0, \sigma_0) = \left( \prod_{j=1}^N \frac{1}{\sqrt{\sigma_0^2 + \sigma_j^2}} \right) \exp \left[ -\frac{1}{2} \sum_{j=1}^N \frac{(B_j - B_0)^2}{\sigma_0^2 + \sigma_j^2} \right]. \quad (8)$$

343 Fig. 4 shows the distribution of  $\mathcal{L}$  as functions of  $B_0$  and  $\sigma_0$  and the probability distributions  
 344 of  $B_0$  and  $\sigma_0$  by integrating  $\mathcal{L}$  along the  $B_0$  axis and the  $\sigma_0$  axis, respectively. The probability  
 345 distribution of  $B_0$  is similar to a normal distribution with a mean value of 4.1  $\mu\text{G}$  and a standard  
 346 deviation of 1.6  $\mu\text{G}$ . The probability distribution of  $\sigma_0$  is highly asymmetric since the values of  $\sigma_0$   
 347 cannot be negative. The first, second, and third quartiles of the  $\sigma_0$  distribution are 0.6, 1.2, and 2.4  
 348  $\mu\text{G}$ . We therefore suspect that the Zeeman measurements in the L1544 envelope can be explain by

349 a magnetic field with  $B_0 = 4.1 \pm 1.6 \mu\text{G}$  and  $\sigma_0 = 1.2^{+1.2}_{-0.6} \mu\text{G}$ .

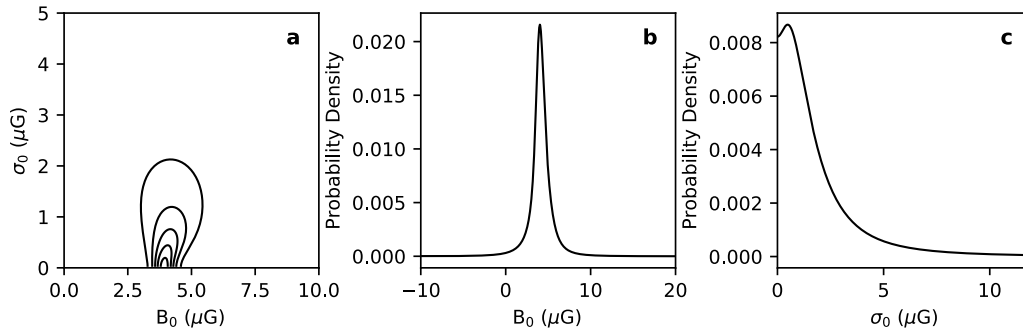


Figure 4: Likelihood  $\mathcal{L}$  for the coherent magnetic field to have mean ( $B_0$ ) and spread ( $\sigma_0$ ) values. **a**, contours of  $\mathcal{L}$  as functions of  $B_0$  and  $\sigma_0$  plotted at 10%, 30%, 50%, 70%, and 90% of the peak value. **b**, the probability distribution of  $B_0$  while allowing all possible values of  $\sigma_0$ . **c**, the probability distribution of  $\sigma_0$  while allowing all possible values of  $B_0$ .

350 **Data availability** FAST raw data are available from the <http://fast.bao.ac.cn> site one year after  
 351 data-taking, per data policy of FAST. Due to the large data volume of this work and the speciality  
 352 of polarization calibration, interested users are encouraged to contact the corresponding author to  
 353 arrange data transfer. The reduced  $I(\nu)$  and  $V(\nu)$  spectra are available at  
 354 <https://github.com/taochung/HINSAzeeman>.

355 **Code availability** The codes analyzing the  $I(\nu)$  and  $V(\nu)$  spectra reported here are available at  
 356 <https://github.com/taochung/HINSAzeeman>. The IDL RHSTK package is available at  
 357 <http://w.astro.berkeley.edu/heiles/>.

359 31. Jiang, P., and 20 colleagues The fundamental performance of FAST with 19-beam receiver at  
 358 L band. *Research in Astronomy and Astrophysics*. 20, (2020).  
 360

- 361 32. Heiles, C., and 9 colleagues Mueller Matrix Parameters for Radio Telescopes and Their Ob-  
362 servational Determination. *PASP*. 113, 1274-1288 (2001).
- 363 33. Jehle, M., M. Ruegg, L. Zuberbuhler, D. Small, and E. Meier Measurement of Ionospheric  
364 Faraday Rotation in Simulated and Real Spaceborne SAR Data. *IEEE Transactions on Geo-*  
365 *science and Remote Sensing*. 47, 1512-1523 (2009).
- 366 34. Perley, R. A. and B. J. Butler Integrated Polarization Properties of 3C48, 3C138, 3C147, and  
367 3C286. *ApJS*. 206, (2013).
- 368 35. McBride, J. and Heiles, C. An Arecibo Survey for Zeeman Splitting in OH Megamaser Galax-  
369 ies. *ApJ*. 763, (2013).
- 370 36. Peek, J. E. G. The Galactic Arecibo L-Band Feed Array Data Release 2: Pipelines and Visu-  
371 alizations. *Astronomical Data Analysis Software and Systems XXV*. 512, 411 (2017).
- 372 37. Griffin, M. J., Abergel, A., Abreu, A., et al. 2010, *A&A*, 518, L3. doi:10.1051/0004-  
373 6361/201014519
- 374 38. Ossenkopf, V. & Henning, T. 1994, *A&A*, 291, 943
- 375 39. Roy, A., André, P., Palmeirim, P., et al. 2014, *A&A*, 562, A138. doi:10.1051/0004-  
376 6361/201322236

# Figures

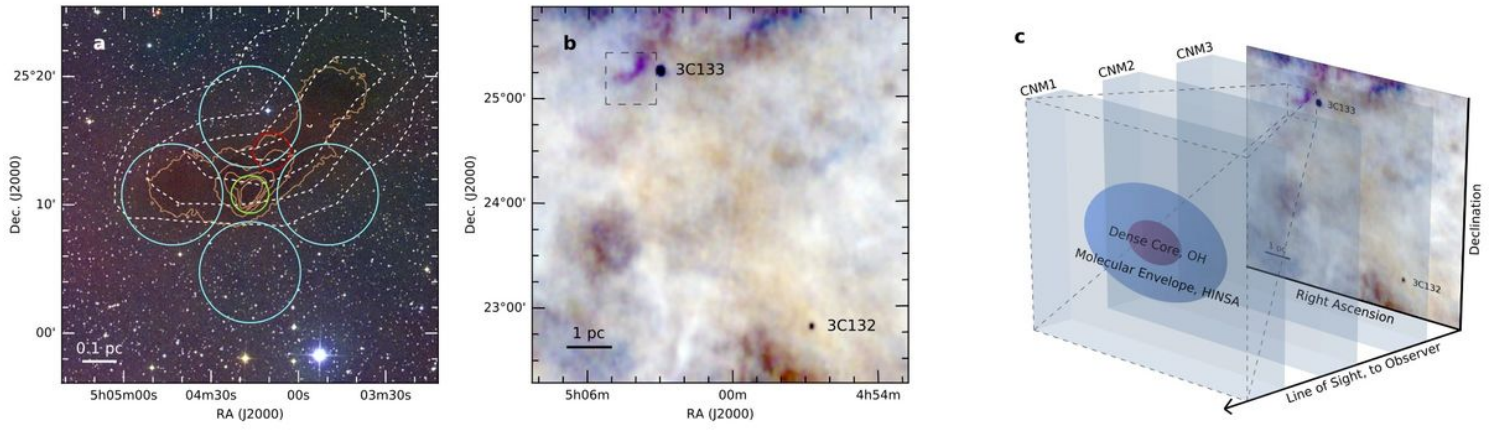
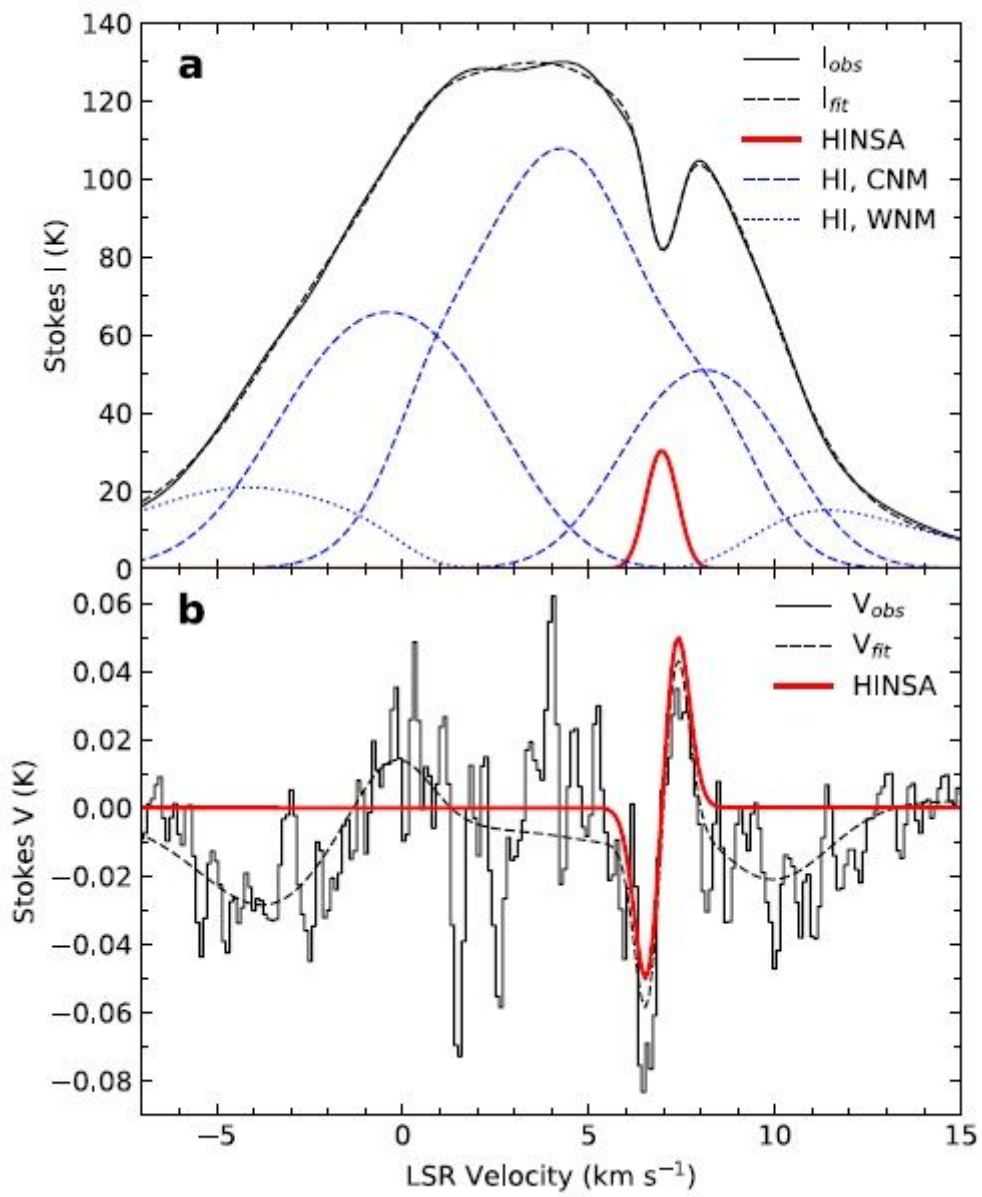


Figure 1

L1544 core and illustration of the structure of interstellar medium from CNM to core (see Manuscript file for full figure legend)



**Figure 2**

The Stokes  $I(v)$  and  $V(v)$  spectra at 21-cm wavelength toward the HINSA column density peak. (see Manuscript file for full figure legend)

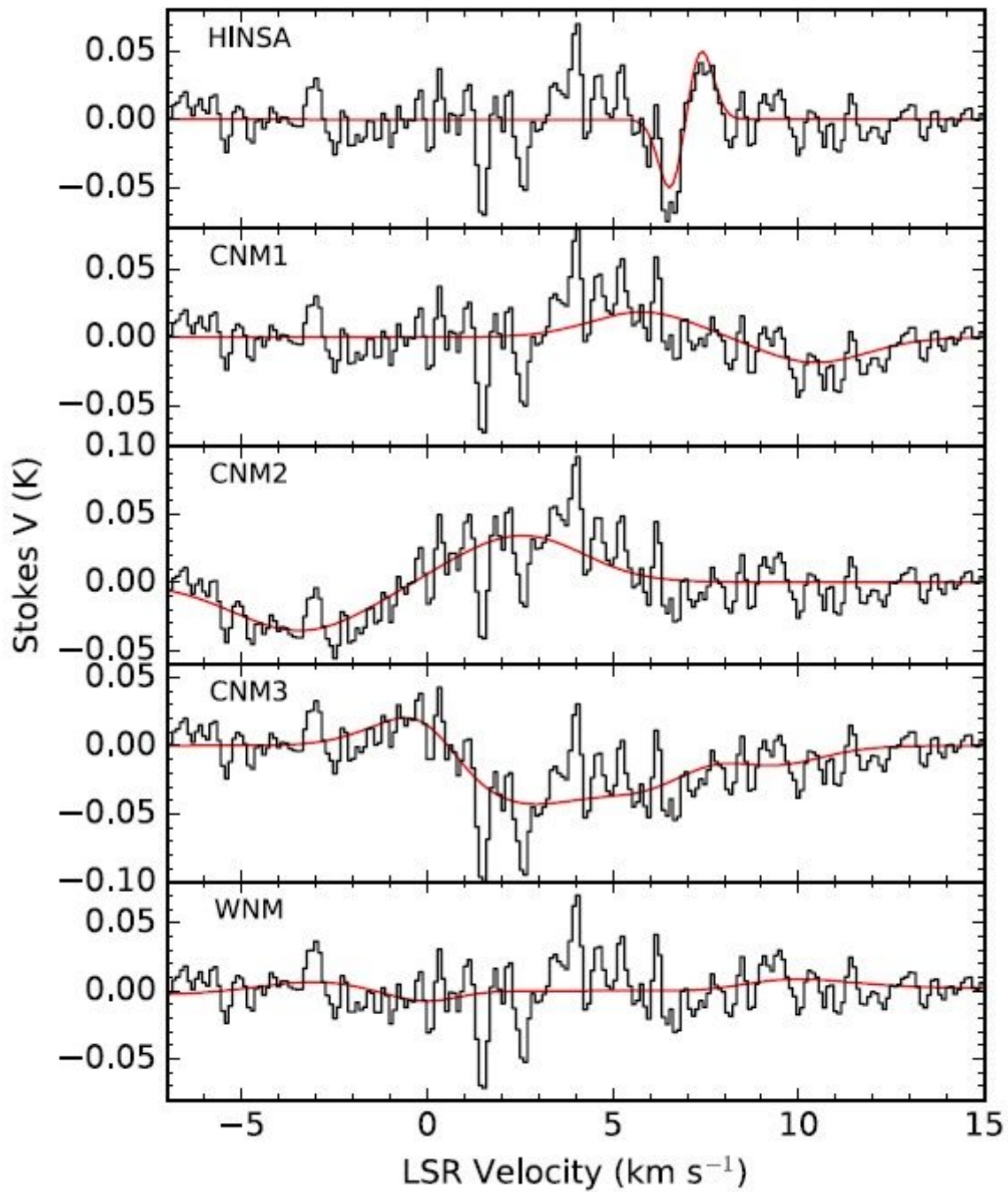


**Figure 3**

The individual  $V(v)$  profiles for the HINSA, CNM, and WNM components. (see Manuscript file for full figure legend)

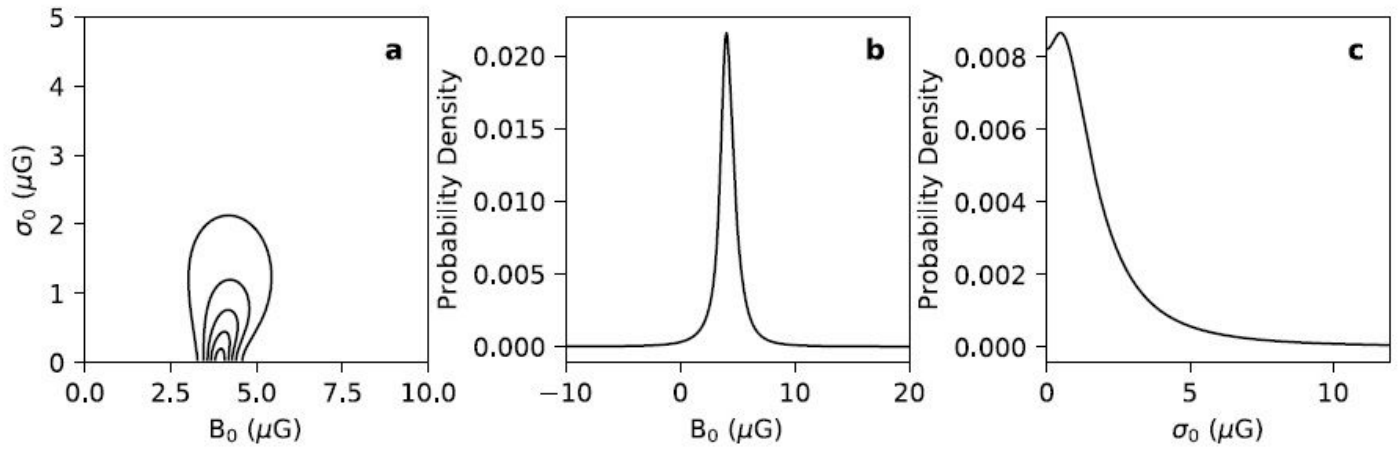


**Figure 4**

Likelihood  $L$  for the coherent magnetic field to have mean ( $B_0$ ) and spread ( $\sigma_0$ ) values. (see Manuscript file for full figure legend)